13C imaging-a new diagnostic platform.

Månsson, Sven; Johansson, Edvin; Magnusson, Peter; Chai, Chun-Ming; Hansson, Georg; Petersson, J Stefan; Ståhlberg, Freddy; Golman, Klaes

Published in:
European Radiology

DOI:
10.1007/s00330-005-2806-x

2006

European Radiology – invited review

^{13}C Imaging—A New Diagnostic Platform

SVEN MÅNSSON[1*], EDVIN JOHANSSON[2], PETER MAGNUSSON[2], CHUN-MING CHAI[3],

GEORG HANSSON[2], J STEFAN PETERSSON[2], FREDDY STÅHLBERG[4],

AND KLAES GOLMAN[2]

[1] *Dept. of Experimental Research, Malmö University Hospital, SE-205 02 Malmö, Sweden*

[2] *Amersham Health R&D AB, Medeon, SE-205 12 Malmö, Sweden*

[3] *Dept. of Diagnostic Radiology, Malmö University Hospital, SE-205 02 Malmö, Sweden*

[4] *Depts. of Diagnostic Radiology and Medical Radiation Physics, Lund University Hospital, SE-221 85 Lund, Sweden*

[*]Corresponding author: Sven Månsson
Dept. of Experimental Research
Malmö University Hospital
SE-205 02 Malmö
Sweden

Email: Sven.Mansson@rontgen.mas.lu.se
Phone +46 40336636
Fax +46 40336207

Running title: ^{13}C Imaging

Abstract

The evolution of magnetic resonance imaging (MRI) has been astounding since the early 1980s, and a broad range of applications has emerged. To date, clinical imaging of nuclei other than protons has been precluded for reasons of sensitivity. However, with the recent development of hyperpolarization techniques, the signal from a given number of nuclei can be increased as much as 100 000 times, sufficient to enable imaging of non-proton nuclei. Technically, imaging of hyperpolarized nuclei offers several unique properties, such as complete lack of background signal and possibility for local and permanent destruction of the signal by means of radio frequency (RF) pulses. These properties allow for improved as well as new techniques within several application areas. Diagnostically, the injected compounds can visualize information about flow, perfusion, excretory function, and metabolic status. In this review article, we explain the concept of hyperpolarization and the techniques to hyperpolarize ^{13}C. An overview of results obtained within angiography, perfusion, and catheter tracking is given, together with a discussion of the particular advantages and limitations. Finally, possible future directions of hyperpolarized ^{13}C MRI are pointed out.

Keywords: Magnetic resonance imaging (MRI); hyperpolarized ^{13}C; new imaging applications; metabolic imaging.

Introduction

The Nuclear Magnetic Resonance (NMR) phenomenon was discovered in the 1940s [1,2], and proposed for imaging purposes three decades later [3]. Since then, Magnetic Resonance Imaging (MRI) has evolved into one of the most powerful techniques in diagnostic clinical medicine and biomedical research. Today, MRI is primarily used as a technique for producing anatomical images, but can also offer functional information on, for instance, motion, flow, perfusion, and diffusion. While MRI reveals soft tissue morphology in detail, MR spectroscopy (MRS) provides information on the physical-chemical state of tissues, and its usefulness as a tool in *in vivo* biological research is clearly established. Spectroscopy of other nuclei than ^{1}H (e.g. ^{31}P, ^{13}C, ^{19}F, ^{23}Na) has extended our knowledge of metabolism; for example, the study of intermediary metabolism of biomolecules has taken new directions by *in vivo* ^{13}C spectroscopy [4].

A fundamental reason for the generally low sensitivity of the NMR technique is the low polarization of the nuclei at thermal equilibrium: even at high magnetic fields, only about 1 of 10^5 nuclei contributes to the detectable signal. In the case of ^{1}H, the low sensitivity is counterbalanced by the high concentration of protons in biological tissues. Compared with ^{1}H, though, the MR sensitivity of ^{13}C is severely impaired due to the lower gyromagnetic ratio of ^{13}C, and the low *in vivo* abundance of the nucleus. For these reasons, clinical imaging applications were in the past restricted to ^{1}H. However, techniques are now available to increase the polarization of selected nuclei by a factor of ~100 000 or more. Using optical pumping techniques, it has accordingly been possible to hyperpolarize noble gases (^{3}He and ^{129}Xe) to an extent that allows for MRI of the airspaces of the lungs [5-8], and the impact of this on the clinical diagnosis of the lung has recently been reviewed [9,10]. Lately, techniques have been developed for hyperpolarization of ^{13}C as well [11,12].

Hyperpolarization versus thermal equilibrium polarization

The principle of NMR is based on the interaction of atomic nuclei with an external magnetic field. A fundamental property of the atomic nucleus is the nuclear spin, and nuclei with non-zero spin can be studied with NMR. Nuclei with spin$=\frac{1}{2}$ (such as ^{1}H (protons) and ^{13}C) orient themselves in two possible directions: parallel ("up"), or anti-parallel ("down") with the external field. The net magnetization per unit volume, and thus the available NMR signal, is proportional to the population difference between the two states. The polarization level is defined as

$$P = \left| \frac{N^+ - N^-}{N^+ + N^-} \right| \tag{1}$$

where N^+ and N^- are number of spins in the "up" and "down" directions, respectively. If the two populations are equal, their magnetic moments cancel, resulting in zero macroscopic magnetization, and thus no NMR signal. However, under thermal equilibrium conditions, slightly higher energy is associated with the "down" direction, and N^- will thus be slightly smaller than N^+ (Fig. 1). For a nucleus with spin$=\frac{1}{2}$, the thermal equilibrium polarization, P_{th}, is given by

$$P_{th} = \tanh\left(\frac{\gamma \hbar B_0}{2 k_B T} \right) \tag{2}$$

where B_0 is the magnetic field strength, γ the gyromagnetic ratio for the nucleus, T the temperature, k_B the Boltzmann constant, and $\hbar$ the Planck constant. As mentioned in the introduction, the thermal equilibrium polarization is very low: even at a magnetic field of 1.5 T it is only $5 \cdot 10^{-6}$ for ^{1}H, and $1 \cdot 10^{-6}$ for ^{13}C (at body temperature).

The signal-to-noise ratio, *SNR*, is proportional to the gyromagnetic ratio, the concentration, c, of the nuclear spins and the polarization

$$SNR \propto c \cdot \gamma \cdot P \tag{3}$$

The fact that the thermal equilibrium polarization increases proportionally with the magnetic field (Eq. (2)), has motivated the development of MRI systems with ever-higher fields. Accordingly, 3 T instruments are nowadays available for clinical whole body imaging [13]. Even higher fields are technically achievable, but practical problems such as radio frequency penetration depths, and tissue contrast, increase rapidly with increasing field.

A different concept to increase the polarization is to create an artificial, non-equilibrium distribution of the nuclei: the "hyperpolarized" state, where the population difference $N^+ - N^-$ is increased by several orders of magnitude compared with the thermal equilibrium (Fig. 1), and independently of the magnetic field strength of the MR imager. The hyperpolarized state of an imaging agent can be created by an external device, followed by rapid administration of the agent to the subject to be imaged. This approach has been used for hyperpolarization of a wide range of organic substances containing ^{13}C, by either para-hydrogen-induced polarization [11] or DNP hyperpolarization [12]. Other nuclei that are feasible for hyperpolarization include ^{3}He, ^{129}Xe and ^{15}N. These methods have in common that the polarization is enhanced by a factor of ~100 000 or more, compared with the thermal equilibrium polarization level (at 1.5 T). The hyperpolarized state has, however, a limited lifetime: once the hyperpolarization has been created, the polarization will strive to return to the thermal equilibrium level, at a rate governed by the T_1 relaxation time. T_1 strongly depends on the chemical structure and environment of the hyperpolarized compound, and for ^{13}C it can typically range from a few seconds to several minutes [14].

Hyperpolarization techniques for ^{13}C

The "brute-force" approach

It follows from Eq. (2) that the thermal equilibrium polarization increases with increasing magnetic field strength and decreasing temperature. A straightforward, "brute-force" approach to increase the polarization in a sample is thus to subject it to a very strong magnetic

field at a temperature close to zero K [15]. For example, by cooling down the sample to liquid helium temperature (4 K) at a field strength of 20 T, the polarization is increased by a factor of 1000. A signal increase by a factor of 1000 is, however, insufficient for clinical ^{13}C applications, and the "brute-force" method would require impractically low temperatures (in the mK range) to be useful.

Dynamic nuclear polarization (DNP)

Under moderate conditions (1 K and 3 T), the ^{13}C nuclear polarization is below 0.1%, whereas the electrons are polarized to >90%, owing to the much larger γ of the electron (c.f. Eq. (2)). Using the dynamic nuclear polarization (DNP) technique, the high polarization of the electron spins can be transferred to coupled nuclear spins [16]. In the method by Ardenkjaer-Larsen *et al.* [12], the material containing the nuclei to be hyperpolarized is doped with a substance containing unpaired electrons, which have a thermal equilibrium polarization of almost unity when exposed to a magnetic field of ~3 T at a temperature of ~1 K. Microwave irradiation near the electron resonance frequency is used to transfer the polarization from the unpaired electrons to the ^{13}C nuclei. Due to the short T_1 of the electrons (~1 μs), the electrons rapidly regain their polarization. By this pumping process, the nuclear polarization in the solid material can be increased to 20–40%. By rapid dissolution, the solid is transformed into an injectable liquid with small polarization losses.

Parahydrogen induced polarization (PHIP)

The parahydrogen induced polarization (PHIP) method increases the nuclear polarization via a chemical reaction involving parahydrogen; a state where the hydrogen nuclei are oriented so that their magnetic moments cancel (Fig. 2a). Bowers and Weitekamp initially predicted and verified that the PHIP effect arises in molecules catalytically hydrogenated with parahydrogen [17,18]. A requisite is that the hydrogenation mechanism operates by transfer of the hydrogen molecule as a unit onto the substrate (Fig. 2b). The non-equilibrium spin order of the parahydrogen molecule can be converted to nuclear polariza-

tion of the ^{13}C nucleus in the substrate, either by means of diabatic-adiabatic field cycling [11,19], or by a sequence of RF-pulses [20], (Fig. 2c).

Imaging of hyperpolarized agents

Properties of hyperpolarized ^{13}C

The ability of conventional ^{1}H MRI to differentiate between various soft tissues and detect pathology is based foremost on the inherently different relaxation times (T_1, T_2, and T_2*) of different tissues, but also on differences in proton density. With the administration of paramagnetic contrast agents, the relaxation rates ($1/T_1$, $1/T_2$) of adjacent protons will increase, related to the concentration of the agent. Depending on the type of imaging sequence, the increased relaxation rates can result in either an increased or a decreased signal where the agent accumulates, thereby increasing the image contrast [21-24].

For hyperpolarized agents, the mechanism is fundamentally different: the hyperpolarized nuclei create the signal themselves, rather than moderating the signal from surrounding protons. The signal strength and the SNR are thus linear functions of the concentration and the polarization level of the hyperpolarized agent (Eq. (3)), contrary to the conventional paramagnetic agents. Furthermore, since the natural abundance of ^{13}C is far below the detection limit of typical imaging protocols, hyperpolarized ^{13}C images completely lack background signal. In this respect, hyperpolarized ^{13}C MRI behaves similarly to modalities such as positron emission tomography (PET) and single photon emission computed tomography (SPECT), where the radiation from the injected tracer is detected, and where the signal amplitude is directly proportional to the concentration of the agent. The lack of background signal is advantageous in many applications, e.g. angiography, where highest possible contrast between vessels and background is desired. On the other hand, without background signal, the anatomical interpretation of the ^{13}C images may be problematic. In such cases,

proton reference images with orientations corresponding to the ^{13}C images must be acquired to provide or increase the anatomical information.

Hyperpolarized ^{13}C has only recently become available at polarization levels adequate for MRI [11,12,19,25,26]. Currently, polarization levels of 20–30% can be obtained by the DNP and PHIP methods, with *in vivo* T_1 and T_2 relaxation times up to ~40 s and ~4 s, respectively. The concentration of a liquid hyperpolarized ^{13}C imaging agent is anticipated to range from 0.3 to 1.2 M in the injection syringe. Due to relaxation and dilution in the vascular system, the estimated first-pass concentration ranges from 2 to 40 mM [24]. This is far below the typical ^{1}H concentration of 80 M, but since the hyperpolarization process can enhance the signal more than 10^5 times, the ^{13}C substance itself can be visualized by ^{13}C MRI within a reasonable time scale. Previously inaccessible changes in molecular structures may thus be monitored.

Considerations for imaging of hyperpolarized ^{13}C

An important characteristic of hyperpolarized MRI, compared to conventional MRI, is that longitudinal magnetization consumed during the imaging process cannot be regained by relaxation processes. Besides the inevitable loss of longitudinal magnetization due to T_1 relaxation, the RF pulses of the imaging sequence will convert unrecoverable longitudinal magnetization to transverse magnetization. Two imaging strategies are therefore possible: either to excite the object with a rapid train of low flip-angle RF pulses, each one destroying only a very small fraction of the available longitudinal magnetization, or to generate the complete image in a single shot (either after one large RF excitation, or by using a train of refocusing RF pulses, which re-uses the transverse magnetization). The low flip-angle approach has commonly been used for hyperpolarized gas imaging [27,28], where the rapid diffusion of the nuclei causes a quick loss of phase coherence (short T_2*) and hence makes it impractical to reuse the magnetization from one phase-encoding step to the next.

With the much longer T_2 relaxation (seconds) of hyperpolarized ^{13}C, it is feasible to use single-shot sequences based on trueFISP, RARE, or EPI, which convert the initial longitudinal magnetization to usable transverse magnetization with nearly 100% efficiency, and thereby give improved SNR. With this technique, it is possible to acquire several images with high temporal resolution to study the distribution of the contrast agent [29]. However, since the gyromagnetic ratio for ^{13}C is four times lower than for ^{1}H, correspondingly stronger gradients are needed, to achieve equal spatial resolution within equal time.

Obviously, the decaying nature of the hyperpolarization restricts the time window for clinical diagnostic imaging to 2–3 times the T_1 relaxation time. For an injected ^{13}C-labeled substance, imaging must thus take place within a few minutes after the injection. An i.v. injected substance reaches the right heart and the lungs in ~4 s, the left heart in ~10 s, and the other major organs in 15–40 s. Most signal will therefore be present in the lungs, the heart, the brain, the liver and the kidneys, at the time of image acquisition.

Clinical applications of hyperpolarized ^{13}C

Vascular imaging with hyperpolarized ^{13}C

The availability of liquid, hyperpolarized compounds with long relaxation times renders "real-time" vascular imaging with hyperpolarized ^{13}C possible, as a new tool to examine pathological conditions. The feasibility of hyperpolarized ^{13}C for MRA has recently been investigated [26,29]. An example of a ^{13}C angiogram, depicting the main arteries of a guinea pig head after i.a. injection in the aortic arch, is shown in Fig. 3. Since the background signal in ^{13}C MR imaging is negligible, the contrast-to-noise ratio (CNR) will be high and, at least initially before the imaging agent has leaked into the extracellular space, the CNR will approach the SNR. Consequently, the vasculature can be visualized using thick imaging slices, or even projection techniques. Fig. 4 shows thick-slice (15 cm) imaging of the coronary arteries in a pig during arterial injection of 5 ml hyperpolarized ^{13}C

through a catheter placed at the LAD. During the injection, trueFISP images were acquired with 300-ms intervals. The main disadvantage of using ^{13}C for angiography, is that the lower gyromagnetic ratio of ^{13}C makes it difficult to achieve a spatial resolution matching proton angiograms, unless the echo and repetition times are substantially prolonged, which in turn may degrade the image quality.

Perfusion imaging

Perfusion measurements with conventional Gd-based MRI contrast agents posses several problems, due to the indirect relationship between signal and tracer concentration. For example, for techniques that rely on the dynamic-susceptibility contrast effect, the tissue's vascular composition also affects the obtained amount of signal [30], and for methods where the T_1-shortening effect of conventional contrast agents is utilized [31], linearity between tracer concentration and signal is typically only present at very low concentrations. As a result, quantification of perfusion is difficult when conventional tracers are employed. If a direct signal source, such as a hyperpolarized ^{13}C tracer, is used, several of these problems are avoided [32]. Compared with traditional tracers, the depolarization of the tracer during the course of the measurement is potentially a complicating factor in the quantitative analysis. However, it has been demonstrated that the assessment of tissue blood flow, in general, is not influenced by the tracer depolarization [32,33].

The ^{13}C tracers investigated so far do not traverse the blood-brain barrier in any significant degree, and therefore are restricted to the vascular bed. As a consequence, the assessment of cerebral perfusion can be expected to be an especially demanding task due to SNR limitations. However, cerebral perfusion has been investigated in rats [32] and theoretical considerations [33] indicate that cerebral perfusion assessment using bolus tracking following venous tracer administration may still be feasible in larger species as well, although the spatial resolution may have to be compromised.

In other tissues such as heart, kidney, and lung, the SNR status is considerably more favorable, since the distribution volumes of the tracer in these tissues are substantially higher. The extraction fractions of the tracers are also expected to be high, due to the low molecular weights of the investigated tracers, although this statement needs further experimental verification. The potential complications emanating from the fact that the tracers reach the interstitial space also requires further investigations. In Fig. 5, the perfusion map from pig myocardium, obtained following venous tracer administration is shown [34].

Besides the traditional models used to evaluate perfusion, as adopted from nuclear medicine, the fact that the spin population of a hyperpolarized tracer is not in thermal equilibrium also makes it possible to assess perfusion in a novel way. In a study performed in rabbit kidneys, it was demonstrated that by repeated RF depolarization of the tracer within the imaging slice, tissue blood flow could be assessed, since the tissue signal thereby only reflects the inflow between successive measurements [35]. The resulting perfusion map is shown in Fig. 6. The perfusion estimates obtained in this way have several attractive properties, such as insensitivity to arterial dispersion and the possibility to determine the influence of noise on the estimates. In addition, the assessment can also be used to derive information about the transit time and the dispersion of the blood in the arteries supplying the investigated tissue.

By administering the tracer via arterial catheters, the dilution of the tracer concentration is reduced. Images obtained following arterial injection of a hyperpolarized tracer, for example acquired as a part of an interventional investigation, therefore exhibit very high SNRs. As a comparison, intraarterial injection would be less beneficial for contrast enhanced ^{1}H perfusion imaging, because very high Gd concentrations typically destroy the signal-concentration linearity and reduce the SNRs. In Fig. 7, examples of relative perfusion maps obtained in this fashion are demonstrated in pig kidney and heart.

Pulmonary circulation and perfusion

MRI measurements of pulmonary perfusion have traditionally been performed either with the arterial spin labeling technique, or with T_1 weighted imaging using the first pass of a Gd-based contrast agent [36]. With the new hyperpolarization techniques, perfusion information can be obtained by direct imaging of the hyperpolarized agent. As an example, lung images of a pig after injection of hyperpolarized ^{13}C are shown in Fig. 8. The images depict the first pass of the hyperpolarized agent in a normal pig (Fig. 8a), and in the same pig after occluding the right pulmonary artery with a balloon catheter (Fig. 8b).

For investigation of lung disease, regional determinations of the ventilation/perfusion ratio ($\dot{V}_A/\dot{Q}$) are of particular interest because of the key role of $\dot{V}_A/\dot{Q}$ in gas exchange [37], and has been the usual initial investigation in patients with suspected pulmonary embolism [38]. The established method to characterize $\dot{V}_A/\dot{Q}$ is the multiple inert-gas-elimination technique (MIGET) [39], which however cannot provide spatial information on the distribution of $\dot{V}_A/\dot{Q}$ within the lung. Recent studies have utilized either SPECT or PET to measure $\dot{V}_A/\dot{Q}$, where the spatial resolution is limited to 1–2 cm^3 at best [40]. Potentially, pulmonary perfusion imaging with hyperpolarized ^{13}C may be used to obtain high-resolution perfusion maps, which in turn may be combined with ventilation data to yield a high-resolution $\dot{V}_A/\dot{Q}$ map. High-resolution ventilation data may be provided e.g. by oxygen-enhanced MRI [41,42] or Xe-enhanced CT [43].

Catheter tracking and visualization

MRI has several advantages as a guidance modality for biopsy procedures: multi planar imaging capabilities enables the catheter to be visualized in three orthogonal planes, lack of ionizing radiation, and both 2D and 3D imaging modes. MRI-based active catheter tracking methods [44,45] may suffer from practical limitations, such as hampered mechanical properties as well as tissue heating caused by the catheter RF-coils [46,47]. Passive tracking methods based on susceptibility-artifacts induced by dysprosium oxide markers depict dis-

crete points along the catheter only [48], and the use of catheter contrast agents with short T_1 relaxation times may suffer from insufficient signal difference between catheter and surrounding tissue [49].

The lack of background signal in hyperpolarized ^{13}C imaging, and consequently the high CNR, makes ^{13}C substances potentially attractive for interventional endovascular MRI procedures [50]. By using a MR system capable of multi-nuclei transmit and receive, ^{13}C catheter images may be acquired simultaneously or interleaved with proton "roadmap" images, followed by on-line image fusion.

Such ^{13}C projection images overlaid on a ^{1}H roadmap may be used directly for interventional guidance. However, multiple 2D projection images of a moving ^{13}C-catheter could also be used for 3D reconstruction of the catheter via back-projection. This will give a direct geometrical correspondence between the ^{13}C catheter and the ^{1}H anatomical roadmap images, where the position of the ^{1}H roadmap image plane could be selected to be at the tip of the catheter. An example of such a 3D catheter reconstruction and image fusion with a subsequently acquired 3D proton roadmap is shown in Fig. 9, where the ^{13}C catheter was traveling through aorta from the aortic arch in a pig.

Another example of ^{13}C catheter tracking in the aorta and renal artery of a pig is shown in Fig. 10. When the catheter tip had reached a position proximal to the right kidney, a few ml of the contrast agent was ejected via a separate channel of the catheter and flushed into the kidney. This shows a potentially clinical important feature, because it is now possible not only to visualize the catheter used for the interventional procedure with high spatial resolution, but also the injected substance. During chemical ablation and therapy, this is a critical factor. By monitoring the passage of the ^{13}C agent through the kidney as shown in Fig. 10, information may additionally be gained about the excretory status of the kidney.

Future directions—metabolic imaging

For metabolic imaging, highly interesting information can be obtained from an NMR-active nucleus, since its resonance frequency is a function of its chemical and physiological environment. This property is utilized in the fields of analytical NMR spectroscopy *in vitro* and clinical MRS *in vivo* [51-53]. Due to SNR limitations, MRS is primarily restricted to protons, ^{19}F, ^{31}P, and ^{23}Na, and to the use of large voxels (~1 cm^3) and long scan times (3–30 min). The spectral information obtained from chemical shift imaging (CSI) is a potential strength of MRI compared to other modalities: while PET and SPECT only reveal the distribution of the active nuclei, regardless if they are still contained within the injected molecules or not, NMR is capable of distinguishing signals from the tracer nuclei in different molecules.

For ^{13}C-labeled compounds, it is mainly the molecular structure that determines the chemical shift. CSI has been used to image the distribution within the brain of metabolites from ^{13}C labeled substances, such as glucose and alanine [54]. Without hyperpolarization, long scan times (minutes) have been required to generate such images. By using the hyperpolarization technique, imaging of the metabolic processes can be accomplished in substantially faster time (seconds). For instance, distribution patterns may be visualized by injection and imaging of several hyperpolarized ^{13}C molecules simultaneously. In this way, valuable information about membrane structure and permeability may be obtained.

With the ability to polarize ^{13}C-labeled substances to >20%, MRI may emerge beyond anatomical (e.g. angiography) and functional (e.g. perfusion and diffusion) visualization. Since hyperpolarized ^{13}C MRI directly gives information about the chemical environment of the hyperpolarized nucleus, investigation of tissue and cell viability (direct molecular imaging) may be feasible.

Conclusion

The availability of injectable, hyperpolarized ^{13}C-substances breaks new ground for MRI. When the RF coils and receivers are tuned to the ^{13}C resonance frequency, the detected signals will come from the injected substance solely. The concept of detecting signals from the injected substance only reminds of PET and SPECT imaging. However, the RF excitation and subsequent signal detection in MRI take place without involving ionizing radiation, contrary to PET and SPECT, where ionizing radiation is emitted by the tracer. It has been demonstrated that hyperpolarized ^{13}C-labeled substances are feasible for several MRI applications. As image modality, MRI combined with a ^{13}C hyperpolarized imaging agent offers the possibility to obtain information about flow, perfusion, and molecular behavior *in vivo*. This novel platform will offer the radiologist new information of importance for medical diagnosis and treatment.

References

1. Bloch F, Hansen WW, Packard M (1946) The nuclear induction experiment. Phys Rev 70:474-485.

2. Purcell EM, Torrey HC, Pound RV (1946) Resonance absorption by nuclear magnetic moments in a solid. Phys Rev 69:37-38.

3. Lauterbur PC (1973) Image formation by induced local interactions: examples employing nuclear magnetic resonance. Nature 242:190-191.

4. Shulman RG, Rothman DL (2001) 13C NMR of intermediary metabolism: implications for systemic physiology. Annu Rev Physiol 63:15-48.

5. Albert MS, Balamore D (1998) Development of hyperpolarized noble gas MRI. Nucl Instrum Methods Phys Res A 402:441-453.

6. Albert MS, Cates GD, Driehuys B, Happer W, Saam B, Springer CS, Jr., Wishnia A (1994) Biological magnetic resonance imaging using laser-polarized ^{129}Xe. Nature 370:199-201.

7. Middleton H, Black RD, Saam B, Cates GD, Cofer GP, Guenther R, Happer W, Hedlund LW, Johnson GA, Juvan K, et al. (1995) MR imaging with hyperpolarized ^{3}He gas. Magn Reson Med 33:271-275.

8. Kauczor H, Surkau R, Roberts T (1998) MRI using hyperpolarized noble gases. Eur Radiol 8:820-827.

9. Kauczor HU (2003) Hyperpolarized helium-3 gas magnetic resonance imaging of the lung. Top Magn Reson Imaging 14:223-230.

10. van Beek EJ, Wild JM, Kauczor HU, Schreiber W, Mugler JP, 3rd, de Lange EE (2004) Functional MRI of the lung using hyperpolarized 3-helium gas. J Magn Reson Imaging 20:540-554.

11. Jóhannesson H, Axelsson O, Karlsson M (2004) Transfer of para-hydrogen spin order into polarization by diabatic field cycling. C R Physique 5:315-324.

12. Ardenkjaer-Larsen JH, Fridlund B, Gram A, Hansson G, Hansson L, Lerche MH, Servin R, Thaning M, Golman K (2003) Increase in signal-to-noise ratio of > 10,000 times in liquid-state NMR. Proc Natl Acad Sci U S A 100:10158-10163.

13. Campeau NG, Huston J, 3rd, Bernstein MA, Lin C, Gibbs GF (2001) Magnetic resonance angiography at 3.0 Tesla: initial clinical experience. Top Magn Reson Imaging 12:183–204.

14. Ardenkjaer-Larsen JH, Axelsson O, Golman K, Wistrand LG, Hansson G, Leunbach I, Petersson JS (1999) Method of magnetic resonance investigation. International patent application no. WO 99/35508.

15. Frossati G (1998) Polarization of ^{3}He, D_2 (and possibly ^{129}Xe) using cryogenic techniques. Nucl Instrum Meth A 402:479-483.

16. Abragam A, Goldman M (1978) Principles of dynamic nuclear polarisation. Rep Prog Phys 41:395–467.

17. Bowers CR, Weitekamp DP (1986) Transformation of symmetrization order to nuclear-spin magnetization by chemical reaction and nuclear magnetic resonance. Phys Rev Lett 57:2645–2648.

18. Bowers CR, Weitekamp DP (1987) Parahydrogen and synthesis allow dramatically enhanced nuclear alignment. J Am Chem Soc 109:5541–5542.

19. Golman K, Axelsson O, Jóhannesson H, Månsson S, Olofsson C, Petersson JS (2001) Parahydrogen-induced polarization in imaging: subsecond ^{13}C angiography. Magn Reson Med 46:1-5.

20. Jóhannesson H, Axelsson O, Karlsson M, Goldman M (2004) Methods to convert para-hydrogen spin order into hetero nuclei polarization for in vivo detection. In: Proc 21st Annual Meeting ESMRMB:144.

21. Prince MR, Yucel EK, Kaufman JA, Harrison DC, Geller SC (1993) Dynamic gadolinium-enhanced three-dimensional abdominal MR arteriography. J Magn Reson Imaging 3:877–881.

22. Merbach A, Tóth É. The Chemistry of Contrast Agents in Medical Magnetic Resonance Imaging. Chichester: John Wiley & Sons; 2001.

23. Nishimura DG, Macovski A, Pauly JM (1986) Magnetic resonance angiography. IEEE Trans Med Imaging 5:140–151.

24. Maki JH, Chenevert TL, Prince MR (1996) Three-dimensional contrast-enhanced MR angiography. Top Magn Reson Imaging 8:322–344.

25. Golman K, Ardenkjaer-Larsen JH, Petersson JS, Månsson S, Leunbach I (2003) Molecular imaging with endogenous substances. Proc Natl Acad Sci U S A 100:10435–10439.

26. Golman K, Ardenkjaer-Larsen JH, Svensson J, Axelsson O, Hansson G, Hansson L, Johannesson H, Leunbach I, Månsson S, Petersson JS, Pettersson G, Servin R, Wistrand LG (2002) ^{13}C-angiography. Acad Radiol 9: Suppl 2, S507–S510.

27. Markstaller K, Eberle B, Schreiber WG, Weiler N, Thelen M, Kauczor HU (2000) Flip angle considerations in (3)helium-MRI. NMR Biomed 13:190–193.

28. Zhao L, Albert MS (1998) Biomedical imaging using hyperpolarized noble gas MRI: pulse sequence considerations. Nucl Instrum Methods Phys Res A 402:454–460.

29. Svensson J, Månsson S, Johansson E, Petersson JS, Olsson LE (2003) Hyperpolarized ^{13}C MR angiography using trueFISP. Magn Reson Med 50:256–262.

30. Kiselev VG (2001) On the theoretical basis of perfusion measurements by dynamic susceptibility contrast MRI. Magn Reson Med 46:1113-1122.

31. Larsson HB, Fritz-Hansen T, Rostrup E, Sondergaard L, Ring P, Henriksen O (1996) Myocardial perfusion modeling using MRI. Magn Reson Med 35:716-726.

32. Johansson E, Månsson S, Wirestam R, Svensson J, Petersson JS, Golman K, Ståhlberg F (2004) Cerebral perfusion assessment by bolus tracking using hyperpolarized ^{13}C. Magn Reson Med 51:464-472.

33. Johansson E (2003) NMR imaging of flow and perfusion using hyperpolarized nuclei. Thesis, Lund University, Sweden.

34. Johansson E, Magnusson P, Chai C-M, Petersson J, Golman K, Wirestam R, Ståhlberg F (2004) Assessing myocardial perfusion using hyperpolarized ^{13}C. In: Proc 21st Annual Meeting ESMRMB:117.

35. Johansson E, Olsson LE, Mansson S, Petersson JS, Golman K, Ståhlberg F, Wirestam R (2004) Perfusion assessment with bolus differentiation: a technique applicable to hyperpolarized tracers. Magn Reson Med 52:1043-1051.

36. Uematsu H, Ohno Y, Hatabu H (2003) Recent advances in magnetic resonance perfusion imaging of the lung. Top Magn Reson Imaging 14:245-251.

37. West JB, Wagner PD (1997) Ventilation-perfusion relationships. In: Crystal RG, West JB, Barnes PJ, Weibel ER (eds) The lung: scientific foundations. Lippincott Williams & Wilkins, Philadelphia, pp 1693-1709.

38. Kearon C (2003) Diagnosis of pulmonary embolism. CMAJ 168:183-194.

39. Wagner PD, Saltzman HA, West JB (1974) Measurement of continuous distributions of ventilation-perfusion ratios: theory. J Appl Physiol 36:588-599.

40. Robertson HT, Glenny RW, Stanford D, McInnes LM, Luchtel DL, Covert D (1997) High-resolution maps of regional ventilation utilizing inhaled fluorescent microspheres. J Appl Physiol 82:943-953.

41. Edelman RR, Hatabu H, Tadamura E, Li W, Prasad PV (1996) Noninvasive assessment of regional ventilation in the human lung using oxygen-enhanced magnetic resonance imaging. Nat Med 2:1236-1239.

42. Ohno Y, Hatabu H, Takenaka D, Adachi S, Van Cauteren M, Sugimura K (2001) Oxygen-enhanced MR ventilation imaging of the lung: preliminary clinical experience in 25 subjects. AJR Am J Roentgenol 177:185-194.

43. Simon BA, Marcucci C, Fung M, Lele SR (1998) Parameter estimation and confidence intervals for Xe-CT ventilation studies: a Monte Carlo approach. J Appl Physiol 84:709-716.

44. Peters DC, Lederman RJ, Dick AJ, Raman VK, Guttman MA, Derbyshire JA, McVeigh ER (2003) Undersampled projection reconstruction for active catheter

imaging with adaptable temporal resolution and catheter-only views. Magn Reson Med 49:216-222.

45. Serfaty JM, Yang X, Aksit P, Quick HH, Solaiyappan M, Atalar E (2000) Toward MRI-guided coronary catheterization: visualization of guiding catheters, guidewires, and anatomy in real time. J Magn Reson Imaging 12:590-594.

46. Wildermuth S, Dumoulin CL, Pfammatter T, Maier SE, Hofmann E, Debatin JF (1998) MR-guided percutaneous angioplasty: assessment of tracking safety, catheter handling and functionality. Cardiovasc Intervent Radiol 21:404-410.

47. Zimmermann-Paul GG, Ladd ME, Pfammatter T, Hilfiker PR, Quick HH, Debatin JF (1998) MR versus fluoroscopic guidance of a catheter/guidewire system: in vitro comparison of steerability. J Magn Reson Imaging 8:1177-1181.

48. Bakker CJ, Hoogeveen RM, Hurtak WF, van Vaals JJ, Viergever MA, Mali WP (1997) MR-guided endovascular interventions: susceptibility-based catheter and near-real-time imaging technique. Radiology 202:273-276.

49. Green JD, Omary RA, Finn JP, Tang R, Li Y, Carr J, Li D (2002) Passive catheter tracking using MRI: comparison of conventional and magnetization-prepared FLASH. J Magn Reson Imaging 16:104-109.

50. Magnusson P, Månsson S, Petersson J, Chai C-M, Hansson G, Johansson E (2004) Passive catheter tracking using MRI and hyperpolarized ^{13}C. In: Proc 21st Annual Meeting ESMRMB:143.

51. Ross B, Michaelis T (1994) Clinical applications of magnetic resonance spectroscopy. Magn Reson Q 10:191–247.

52. Cousins JP (1995) Clinical MR spectroscopy: fundamentals, current applications, and future potential. AJR Am J Roentgenol 164:1337–1347.

53. Henriksen O (1994) MR spectroscopy in clinical research. Acta Radiol 35:96–116.

54. Sonnewald U, Gribbestad IS, Westergaard N, Nilsen G, Unsgard G, Schousboe A, Petersen SB (1994) Nuclear magnetic resonance spectroscopy: biochemical evaluation of brain function in vivo and in vitro. Neurotoxicology 15:579–590.

55. Kety SS, Schmidt CF (1948) The nitrous oxide method for the quantitative determination of cerebral blood flow in man: theory, procedure and normal values. J Clin Invest 27:476-483.

Figure legends

Fig. 1. Pictorial description of the orientation of the nuclei at thermal equilibrium and in the hyperpolarized state. In the figure, the magnetic field (B_0) is directed vertically upwards.

Fig. 2. a) The four possible orientations of the nuclear spin in the hydrogen molecule. b) A substrate molecule containing e.g. ^{13}C is hydrogenated with parahydrogen. c) The spin order of the parahydrogen molecule is converted to nuclear polarization of the ^{13}C nucleus, via a diabatic field cycling scheme.

Fig. 3. Angiogram depicting the arteries in a guinea pig head. The image was acquired after intraarterial injection of ^{13}C, hyperpolarized with the PHIP method. The pulse sequence was a projection trueFISP with 500 ms scan time.

Fig. 4. The coronary arteries of a pig, visualized during arterial catheter injection of hyperpolarized ^{13}C. TrueFISP images with 300 ms scan time were acquired continuously during the infusion (0.6 ml/s). The slice thickness was 15 cm. The rightmost X-ray image shows the position of the catheter and the coronary arteries after injection of X-ray contrast media.

Fig. 5. Quantitative myocardial perfusion map in pig, obtained after venous administration of PHIP-polarized 2-hydroxyethylacrylate (0.35 M, 0.2 mmol/kg). The map (in color) was determined from a series of ECG-gated trueFISP images via curve fitting using the Kety-Schmidt technique [55] and is overlaid on a proton image. The trueFISP images were acquired with ≈2-s intervals.

Fig. 6. Quantitative perfusion map of the renal cortex in rabbit. The map was obtained from a series of trueFISP images, which repeatedly destroy the polarization within the slice (1.5 s between images). The compound 2-hydroxyethylacrylate was polarized using the PHIP method and injected via an ear vein (0.30 M, 0.3 mmol/kg).

Fig. 7. TrueFISP ^{13}C images of the renal cortex (a) and myocardium (b) in pig acquired directly after intraarterial administration of 2-hydroxyethylacrylate in the renal artery, and in the LAD and CX, respectively. The slice thickness is 1 cm in both images. Since tracer outflow is expected to be negligible, the images represent relative perfusion maps of the two tissues.

Fig. 8. TrueFISP ^{13}C images of pig lungs. Images show the first pass of PHIP hyperpolarized 2-hydroxyethylacrylate in normal lungs (a) and after occlusion of the right pulmonary artery with a balloon catheter (b). The bright signals visible in the left lung originate from blood in the left ventricle and the aorta.

Fig. 9. ^{13}C catheter tracking along the aorta of a pig. The catheter was flushed with hyperpolarized ^{13}C and images were acquired with a frame rate of 2 projections/s. Using projection imaging, the catheter is visualized without background (a). A 3D representation of the catheter was reconstructed from two orthogonal ^{13}C projections and merged with a 3D ^{1}H roadmap. The catheter (color) may be visualized in a slice though the volume (b), or as a maximum intensity projection (c).

Fig. 10. Catheter tracking of the renal arteries in pig. A bolus of 2-hydroxyethylacrylate was injected into the kidney via a separate channel of the catheter. The ^{13}C image series (color) was acquired using a TrueFISP sequence with in-plane resolution 2×2 mm^2 and acquisition time 329 ms/image. Because the images were acquired as coronal projections, the renal cortex is visible throughout the kidney, as opposed to the kidney image in Fig. 7, which has a slice thickness of 1 cm.

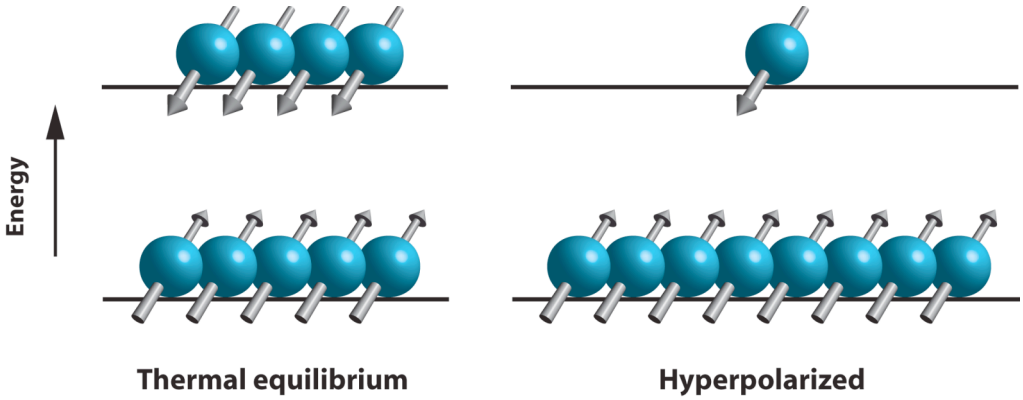

Fig. 1

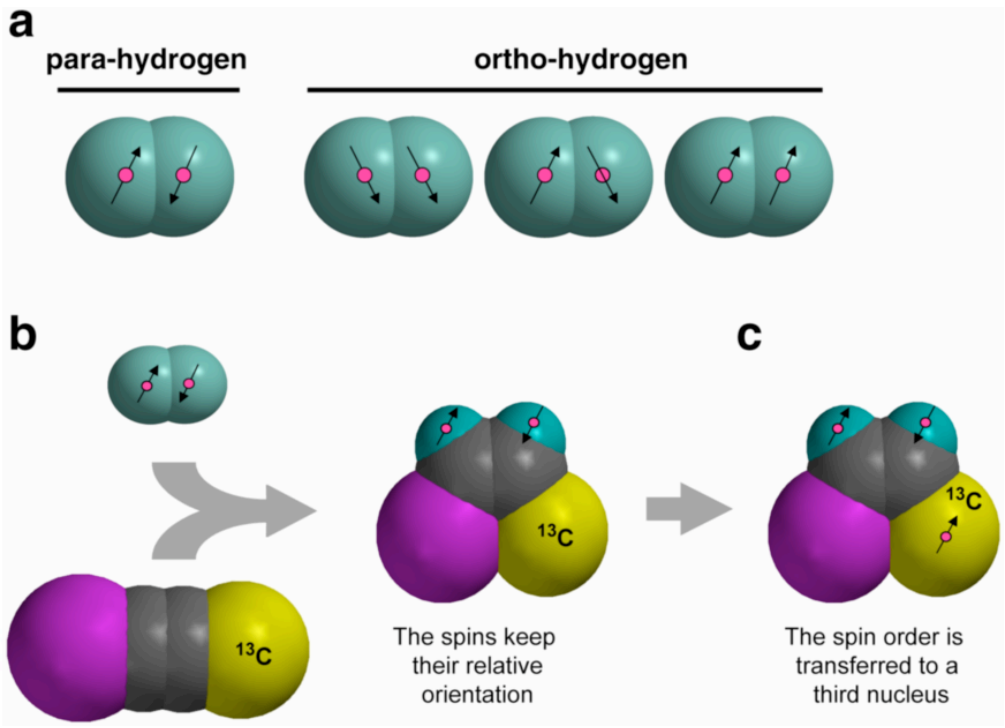
a
para-hydrogen
ortho-hydrogen
b
c
^{13}C
^{13}C
^{13}C
The spins keep their relative orientation
The spin order is transferred to a third nucleus

Fig. 2

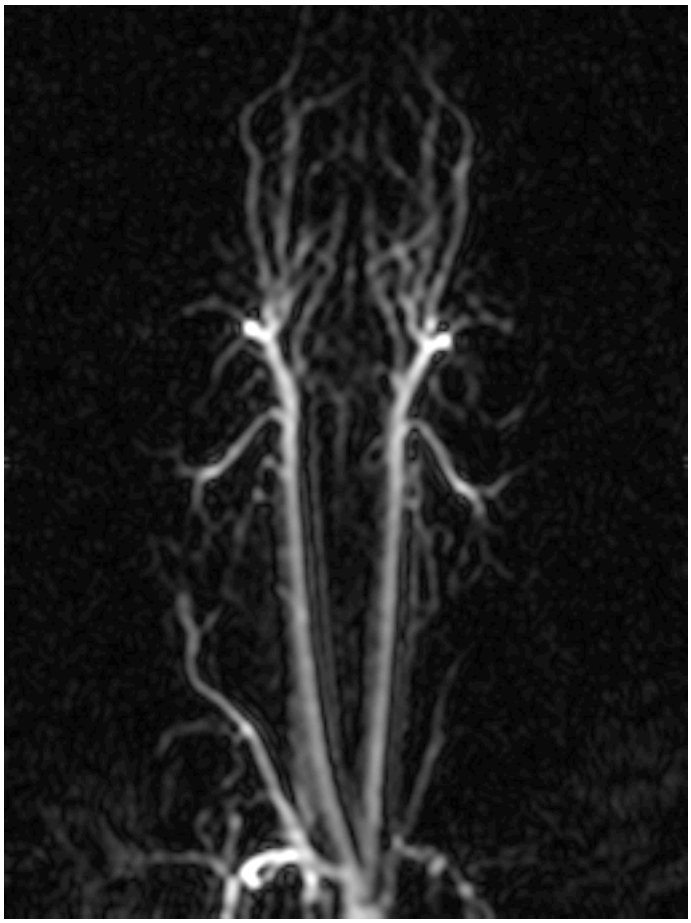

Fig. 3

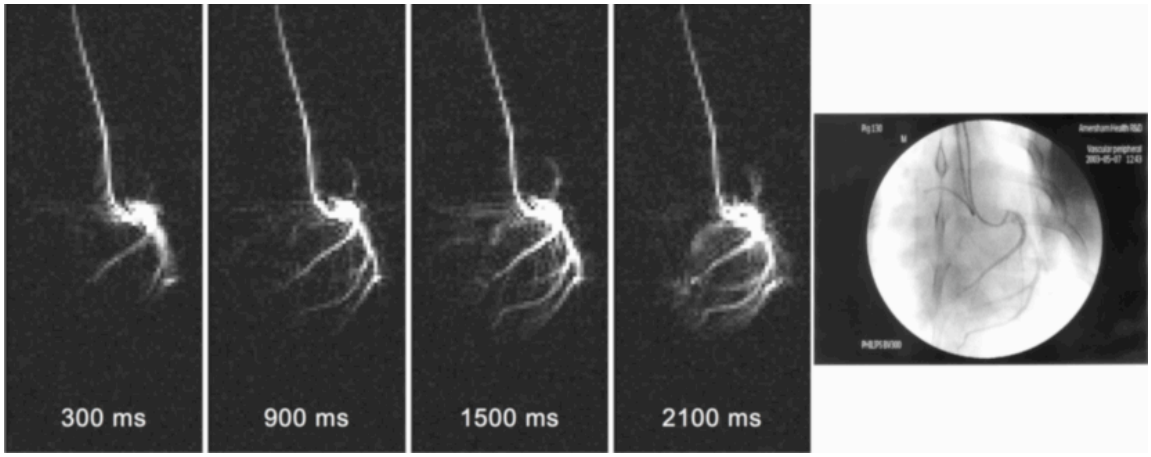

Fig. 4

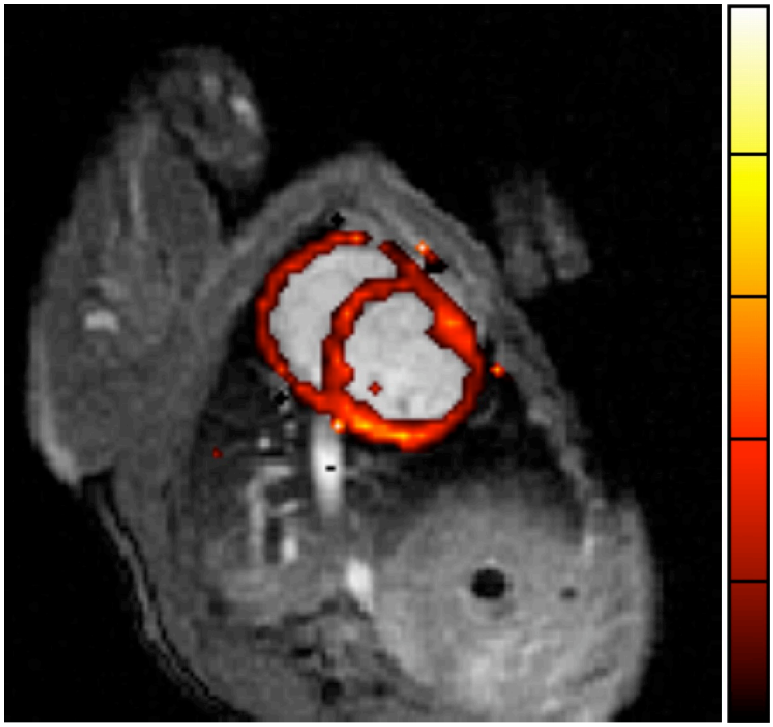

Fig. 5

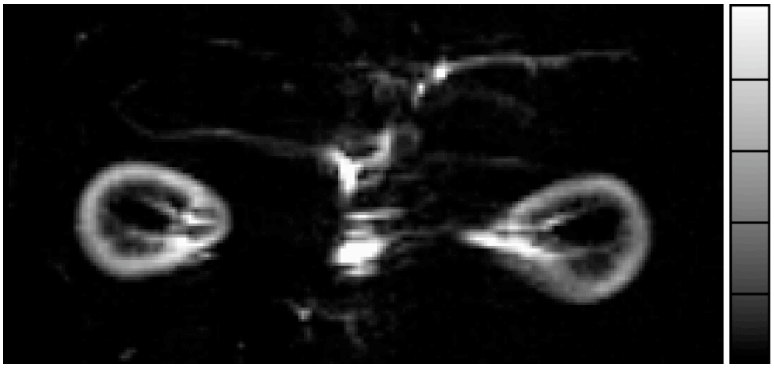

Fig. 6

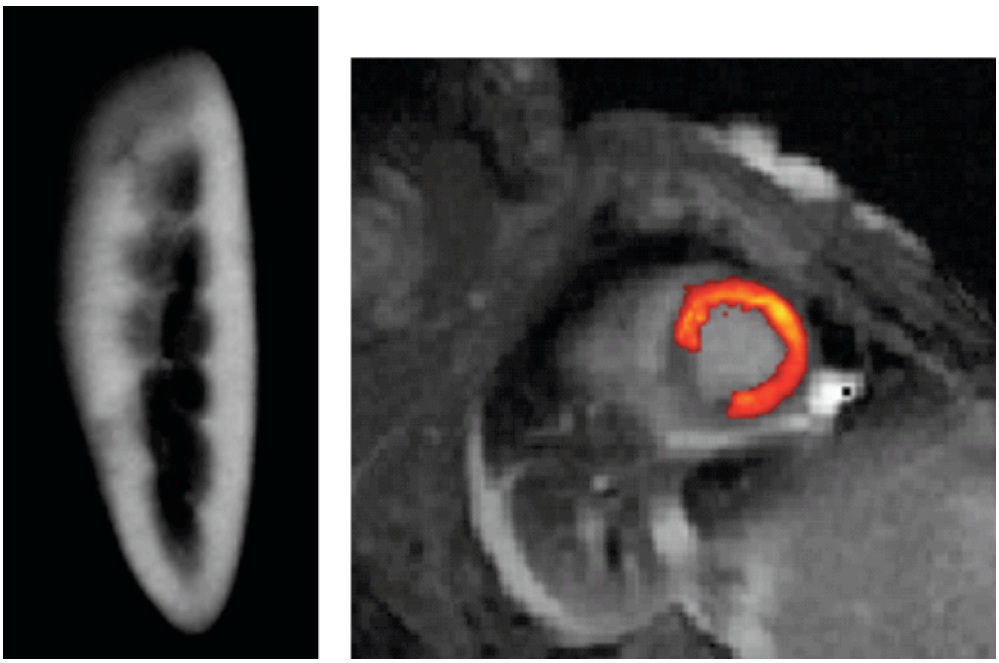

Fig. 7

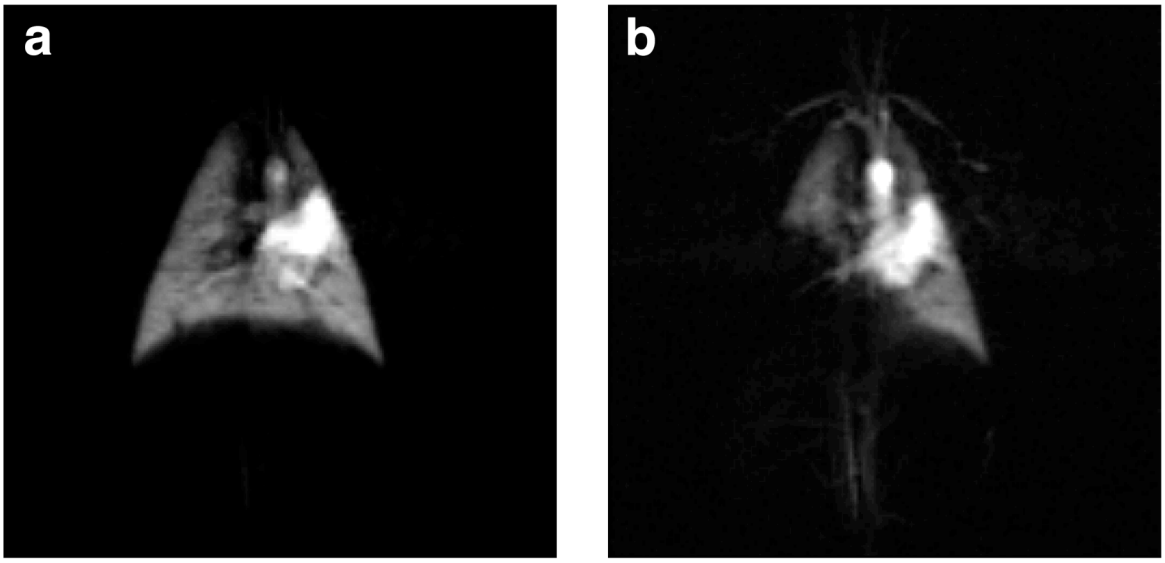

Fig. 8

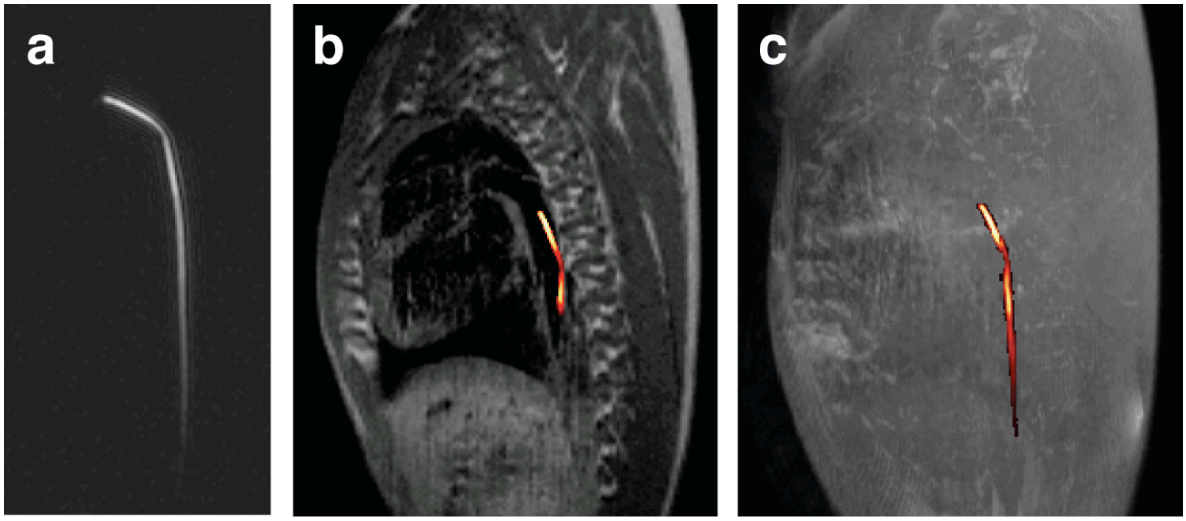

Fig. 9

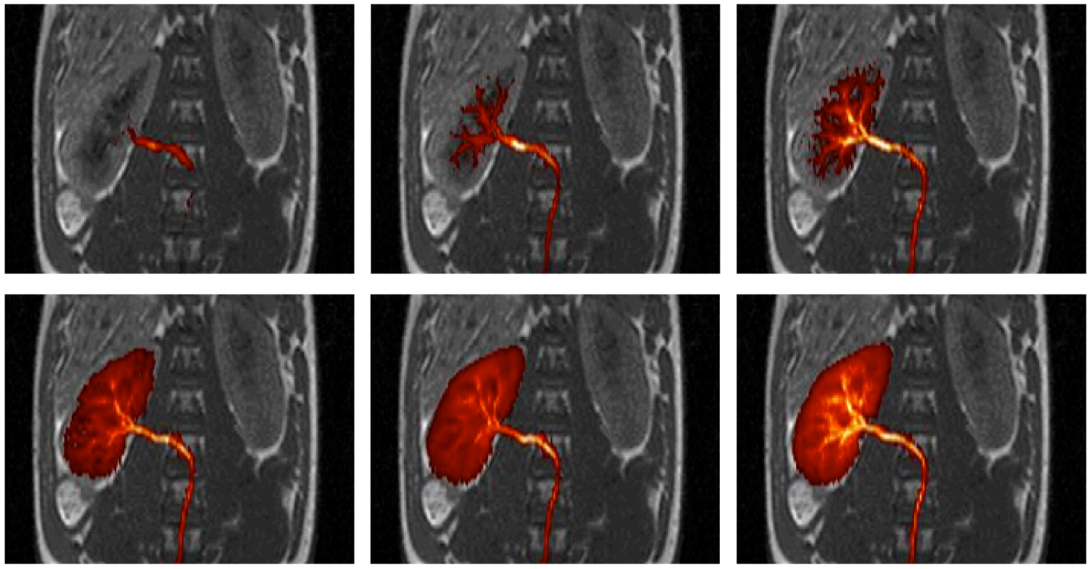

Fig. 10